

**Microscopic optical potential for  ${}^6\text{He}$** Hairui Guo,<sup>1,\*</sup> Haiying Liang,<sup>2</sup> Yongli Xu,<sup>3</sup> Yinlu Han,<sup>2,†</sup> Qingbiao Shen,<sup>2</sup> Chonghai Cai,<sup>4</sup> and Tao Ye<sup>1</sup><sup>1</sup>*Institute of Applied Physics and Computational Mathematics, Beijing 100094, China*<sup>2</sup>*Key Laboratory of Nuclear Data, China Institute of Atomic Energy, P.O. Box 275(41), Beijing 102413, China*<sup>3</sup>*College of Physics and Electronic Science, Shanxi Datong University, Datong 037009, China*<sup>4</sup>*College of Physics, Nankai University, Tianjin 300071, China*

(Received 21 April 2016; revised manuscript received 19 February 2017; published 27 March 2017)

The microscopic optical potential for  ${}^6\text{He}$  with no free parameters is obtained by folding the microscopic optical potentials of its constituent nucleons with the internal wave function of  ${}^6\text{He}$ . We use the isospin-dependent nucleon microscopic optical potential, which is derived by using the Green's function method through the nuclear matter approximation and the local density approximation based on the Skyrme nucleon-nucleon effective interaction. The internal wave function of  ${}^6\text{He}$  is described in a harmonic-oscillator form. The  ${}^6\text{He}$  microscopic optical potential is used to calculate the reaction cross sections and elastic-scattering angular distributions for target nuclei in the mass range  $12 \leq A \leq 209$  at incident energies up to 350 MeV. The results are compared with the experimental data and those calculated by a global phenomenological optical potential; in most cases, the microscopic optical potential reproduces the experimental data less well than the global potential. The sensitivity of scattering to the potentials as a function of radius has been investigated by using the notch perturbation method. The investigation shows that the scattering is sensitive to the optical potential in the nuclear surface region. It is concluded from the discussion that the microscopic optical potential can be improved by increasing the surface absorption contribution.

DOI: [10.1103/PhysRevC.95.034614](https://doi.org/10.1103/PhysRevC.95.034614)**I. INTRODUCTION**

Optical potentials are the basis and starting point of the nuclear reaction analysis, which can not only predict total reaction cross sections and elastic-scattering angular distribution directly, but also play an essential role in the description of inelastic scattering process, transfer reaction and compound nucleus reaction. The microscopic optical potential (MOP) is generated theoretically based on the nucleon-nucleon ( $NN$ ) interaction, it need not be determined by adjusting parameters to fit the available experimental data as the phenomenological optical potential does. As a result, it has no free parameters and does not rely on the experimental data. Therefore, microscopic derivation of optical potentials is a goal of nuclear reaction theory, which has great significance in nuclear reaction analysis, especially in the study of the nuclear reactions including unstable nuclei because the elastic-scattering measurement of unstable nuclei is difficult.

${}^6\text{He}$  is an interesting nucleus because it is a participant in the helium-burning reaction chains in nucleosynthesis and is one of the lightest nuclei with a halo structure. With the development of facilities that produce radioactive ion beams, some measurements [1–20] for  ${}^6\text{He}$  scattering were performed. In most cases, phenomenological optical potentials [4,13,14,19] with the Woods–Saxon form were used to analyze the experimental data. In addition, a few of semimicroscopic [5,10] optical potentials were also developed, the real parts of which were obtained by folding model and the imaginary parts were still phenomenological ones. All of these optical

potentials have some adjustable parameters, and most are for one target nucleus or one incident energy point, which cannot be applied to the other target nuclei or incident energies. Kucuk *et al.* [21] provided a global phenomenological  ${}^6\text{He}$  optical potential (GOP) based on experimental data, which could be used for target nuclei from  ${}^{12}\text{C}$  to  ${}^{209}\text{Bi}$  and low incident energies below 50 MeV. Recently, Su *et al.* [22] also obtained a GOP by fitting the existing experimental data for incident energies up to 250 MeV. The extent of the agreement between the calculated results by both GOPs and the experimental data is similar. As is known, the more experimental data there are, the more reliable the prediction of GOP is for cases without experimental data. Since  ${}^6\text{He}$  is an unstable nucleus and the measurement of  ${}^6\text{He}$  scattering from target nuclei is difficult, we hope to develop a microscopic  ${}^6\text{He}$  optical potential for understanding the  ${}^6\text{He}$ -nucleus interaction, predicting the elastic-scattering data in a wide range of target nuclei and incident energies, and analyzing the nuclear reactions in which  ${}^6\text{He}$  participates in the entrance or exit channel. The purpose of this paper is to obtain a  ${}^6\text{He}$  MOP with no free parameters for a wide range of target nuclei and incident energies.

In our previous work, the MOPs for nucleon [23], deuteron [24], triton [25], helium-3 [26], and alpha [27] were obtained by using the Green's function method and the folding model [28–30]. The folding model is a powerful tool to derive optical potentials for complex nuclei. In the model, the optical potential for a composite nucleus is considered as the sum of the optical potentials for its constituent nucleons averaged over their internal motion within the composite particle. This means that the MOP for  ${}^6\text{He}$  can be obtained by folding the MOPs of its constituent nucleons with their probability distribution in  ${}^6\text{He}$ . We have developed an isospin-dependent nonrelativistic nucleon MOP [23] by using the Green's function method

\*guo\_hairui@iapcm.ac.cn

†hanyl@ciae.ac.cn

on the base of the Skyrme nucleon-nucleon interaction. It is expressed analytically and can reproduce the experimental data fairly well. The internal wave function of  ${}^6\text{He}$  can be described by using a harmonic-oscillator potential. Thus, the MOP for  ${}^6\text{He}$  is derived by using the folding model based on the isospin-dependent nonrelativistic nucleon MOP with the internal wave function of  ${}^6\text{He}$  described in harmonic oscillator form. To check the predictive power and the reliability of the  ${}^6\text{He}$  MOP, it is applied to calculate the reaction cross section and the elastic-scattering angular distributions for the target nuclei from  ${}^9\text{Be}$  to  ${}^{209}\text{Bi}$  at incident energies up to 350 MeV, and the results are compared with experimental data.

In Sec. II, the formulation of the  ${}^6\text{He}$  MOP is presented. In Sec. III, theoretical results are compared with experimental data and discussed. Finally, Sec. IV is a summary.

## II. THEORETICAL MODEL

In the folding model, the optical potential for  ${}^6\text{He}$  is expressed as

$$V(R) = \int \varphi^*(\xi) \left( \sum_{i \in P} V_i \right) \varphi(\xi) d\xi, \quad (1)$$

where  $R$  is the relative coordinate between the centers of mass of  ${}^6\text{He}$  and the target nucleus, and  $\xi$  denotes the internal coordinates of  ${}^6\text{He}$ .  $V_i$  is the optical potential between the nucleon  $i$  in  ${}^6\text{He}$  and the target nucleus with the nucleon energy being one sixth of the incident  ${}^6\text{He}$  energy.  $\varphi(\xi)$  is the internal wave function of  ${}^6\text{He}$ .

In this paper,  $V_i$  is described by the isospin-dependent nonrelativistic nucleon MOP taken from Ref. [23]. We show the detail of the derivation of the nucleon MOP in Ref. [23], so just a brief introduction is given here. From the viewpoint of many-body theory, the nucleon optical potential can be identified with the mass operator of the one-particle Green's function [31]. The first- and second-order mass operators of the one-particle Green's function in nuclear matter were derived based on the Skyrme nucleon-nucleon effective interaction, GS2 [32]. The first-order mass operator was used to denote the real part of the nucleon MOP, and the imaginary part of the second-order mass operator denotes the imaginary part of the nucleon MOP. The MOP for finite target nuclei was then obtained by applying a local density approximation [33]. The nucleon MOP is isospin-dependent and expressed analytically, which can reproduce the experimental data fairly well [23].

${}^6\text{He}$  is a  $1p$ -shell nucleus, two protons and two neutrons within  ${}^6\text{He}$  locate at the  $1s$  state, the other two neutrons locate at the  $1p$  state. The harmonic-oscillator radial wave function of the  $1s$ -state single nucleon is expressed as

$$\phi_s(r) = 2\sqrt{\pi} \left( \frac{\beta}{\pi} \right)^{\frac{3}{4}} \exp\left(-\frac{\beta}{2}r^2\right), \quad (2)$$

while the harmonic-oscillator radial wave function of  $1p$ -state single nucleon is expressed as

$$\phi_p(r) = \beta \left( \frac{64\beta}{9\pi} \right)^{\frac{1}{4}} r \exp\left(-\frac{\beta}{2}r^2\right), \quad (3)$$

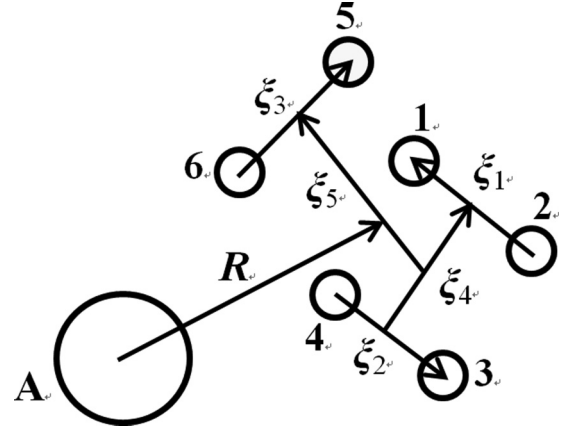


FIG. 1. The relation of the coordinates of each nucleon in  ${}^6\text{He}$  with the internal relative coordinates  $\xi$ .

where  $\beta$  is the parameter of the harmonic-oscillator potential and is defined by

$$\beta = \frac{m\omega}{\hbar}, \quad (4)$$

with  $m$  being the mass of the nucleon and  $\omega$  being the frequency of the harmonic oscillator.

The relation of the coordinates  $r_1, r_2, r_3, r_4, r_5$ , and  $r_6$  of each nucleon in  ${}^6\text{He}$  with the internal relative coordinates  $\xi$  ( $\xi_1, \xi_2, \xi_3, \xi_4, \xi_5$ ) is shown in Fig. 1 and denoted as

$$\begin{aligned} r_1 &= R - \frac{1}{3}\xi_5 + \frac{1}{2}\xi_4 + \frac{1}{2}\xi_1, \\ r_2 &= R - \frac{1}{3}\xi_5 + \frac{1}{2}\xi_4 - \frac{1}{2}\xi_1, \\ r_3 &= R - \frac{1}{3}\xi_5 - \frac{1}{2}\xi_4 + \frac{1}{2}\xi_2, \\ r_4 &= R - \frac{1}{3}\xi_5 - \frac{1}{2}\xi_4 - \frac{1}{2}\xi_2, \\ r_5 &= R + \frac{2}{3}\xi_5 + \frac{1}{2}\xi_3, \\ r_6 &= R + \frac{2}{3}\xi_5 - \frac{1}{2}\xi_3. \end{aligned} \quad (5)$$

The internal wave function of  ${}^6\text{He}$  is described as the harmonic-oscillator wave function of the six-particle system written as

$$\begin{aligned} \varphi(\xi) &= \left( \frac{\beta^5}{6\pi^5} \right)^{\frac{3}{4}} \left( \frac{48}{29} \right)^{\frac{1}{2}} \beta \left( \frac{4}{9}\xi_5^2 - \frac{1}{4}\xi_3^2 \right) \\ &\times \exp\left(-\frac{\beta}{4}\xi_1^2 - \frac{\beta}{4}\xi_2^2 - \frac{\beta}{4}\xi_3^2 - \frac{\beta}{2}\xi_4^2 - \frac{2\beta}{3}\xi_5^2\right). \end{aligned} \quad (6)$$

The parameter  $\beta$  is determined by

$$r_m = \frac{1}{6} \int \sum_{i=1}^6 (r_i - R)^2 |\varphi(\xi)|^2 d\xi, \quad (7)$$

where  $r_m$  is the matter root-mean-square radius of  ${}^6\text{He}$ . The value of  $r_m$  is taken from Ref. [34], where  $r_m$  was set as 2.57 fm by fitting the measured interaction cross sections. Thus, the corresponding value of  $\beta$  is 0.2397.

To get a more intuitive view of the  ${}^6\text{He}$  structure, the radial probability distributions ( $P$ ) of  $1s$ -state protons or

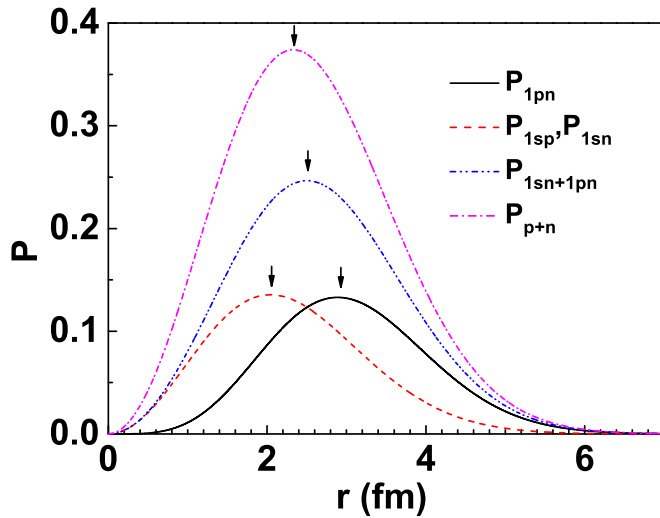


FIG. 2. Radial probability distributions of  $1s$ -state protons and neutrons (dashed line),  $1p$ -state neutrons (solid line), all neutrons (dash-dot-dotted line), and all nucleons (dash-dotted line) relative to the full nucleon probability distribution of  ${}^6\text{He}$ . The arrows denote the corresponding most-probable radii.

neutrons ( $P_{1sp}$  or  $P_{1sn}$ ),  $1p$ -state neutrons ( $P_{1pn}$ ), all neutrons ( $P_{1sn+1pn}$ ), and all nucleons ( $P_{p+n}$ ) relative to the full nucleon probability distribution of  ${}^6\text{He}$  are calculated.  $P_{1sp}$  and  $P_{1sn}$  are expressed as

$$P_{1sp} = P_{1sn} = \frac{1}{3} |\phi_s(r)|^2 r^2, \quad (8)$$

$P_{1pn}$  is expressed as

$$P_{1pn} = \frac{1}{3} |\phi_p(r)|^2 r^2, \quad (9)$$

$P_{1sn+1pn}$  is expressed as  $P_{1sn+1pn} = P_{1sn} + P_{1pn}$ , and  $P_{p+n}$  is expressed as  $P_{p+n} = 2P_{1sn} + P_{1pn}$ . The calculated results are shown in Fig. 2. It can be seen that the  $1p$ -state neutrons tend to distribute farther than  $1s$ -state nucleons. The arrows in the figure denote the most probable radii which are determined by

$$\frac{d}{dr} P = 0. \quad (10)$$

The most probable radius of  $1p$ -state neutrons (2.9 fm) is much larger than that of  $1s$ -state nucleons (2.04 fm), as a result, the  $1p$ -state neutrons distribute mainly in the outer region of the nucleus, like a halo.

### III. CALCULATED RESULTS AND ANALYSIS

The  ${}^6\text{He}$  MOP obtained in Sec. II is analyzed and used to predict the reaction cross sections and elastic-scattering angular distributions for different target nuclei from  ${}^{12}\text{C}$  to  ${}^{209}\text{Bi}$ . The calculated results denoted by the solid lines are compared with the existing experimental data in the following figures.

The radial dependence of the real and imaginary parts of the  ${}^6\text{He}$  MOP for  ${}^{208}\text{Pb}$  at incident energies of 45, 155, and 300 MeV is shown in Fig. 3. It can be seen that the absolute value of the real part decreases with increas-

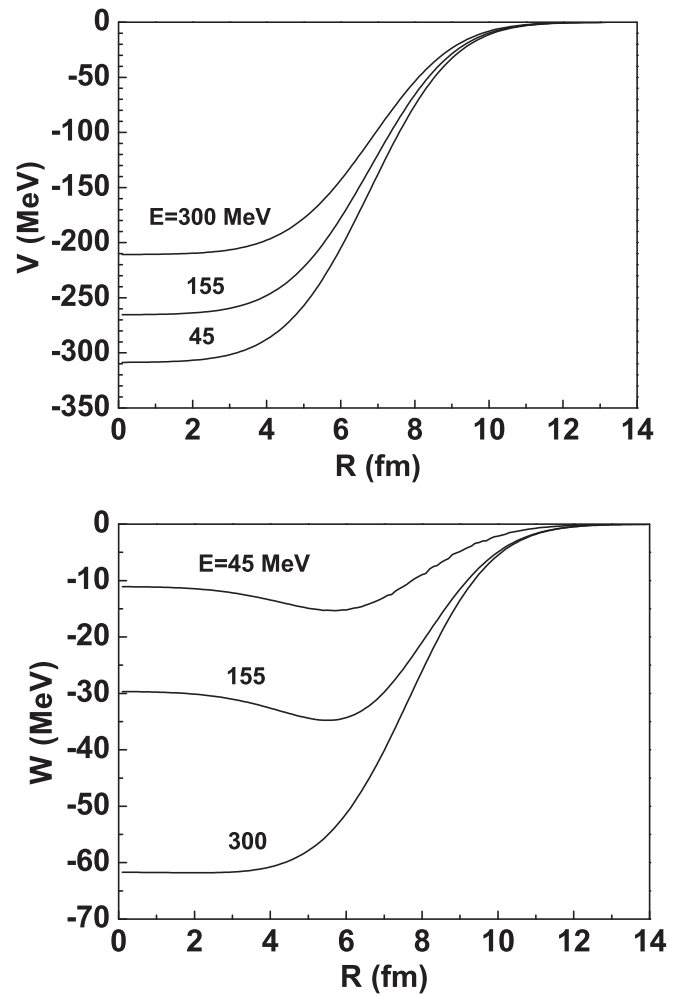


FIG. 3. Radial dependence of the MOP for  ${}^6\text{He} + {}^{208}\text{Pb}$  reaction.

ing radius and incident energy, while the absolute value of the imaginary part increases with increasing energy of incident  ${}^6\text{He}$ .

The calculated result of the differential cross section relative to Rutherford cross section for  ${}^6\text{He}$  elastic scattering from  ${}^{12}\text{C}$  at incident energies from 8.79 to 250 MeV is compared with the experimental data [3–6] in Fig. 4. The calculated result basically reproduces the experimental data except at 18.0 MeV. The reason for the discrepancy may be that the light nuclei have a strong nuclear-structure effect at low incident energy and the nuclear matter approximation used in the derivation of the nucleon MOP cannot describe it well.

Figure 5 shows the differential cross section relative to Rutherford cross section for  ${}^6\text{He}$  elastic scattering from  ${}^{27}\text{Al}$  at incident energies from 9.54 to 13.4 MeV. The theoretical result is in reasonable agreement with the experimental data [7].

Figures 6–9 show the angular distributions of  ${}^6\text{He}$  elastic scattering from the four medium-mass nuclei  ${}^{51}\text{V}$ ,  ${}^{58}\text{Ni}$ ,  ${}^{65}\text{Cu}$ , and  ${}^{64}\text{Zn}$ , respectively. The theoretical results are a little lower than the experimental data [8–13] for some relatively larger angles.

The calculated result of the differential cross section relative to Rutherford cross section for  ${}^6\text{He}$  elastic scattering from

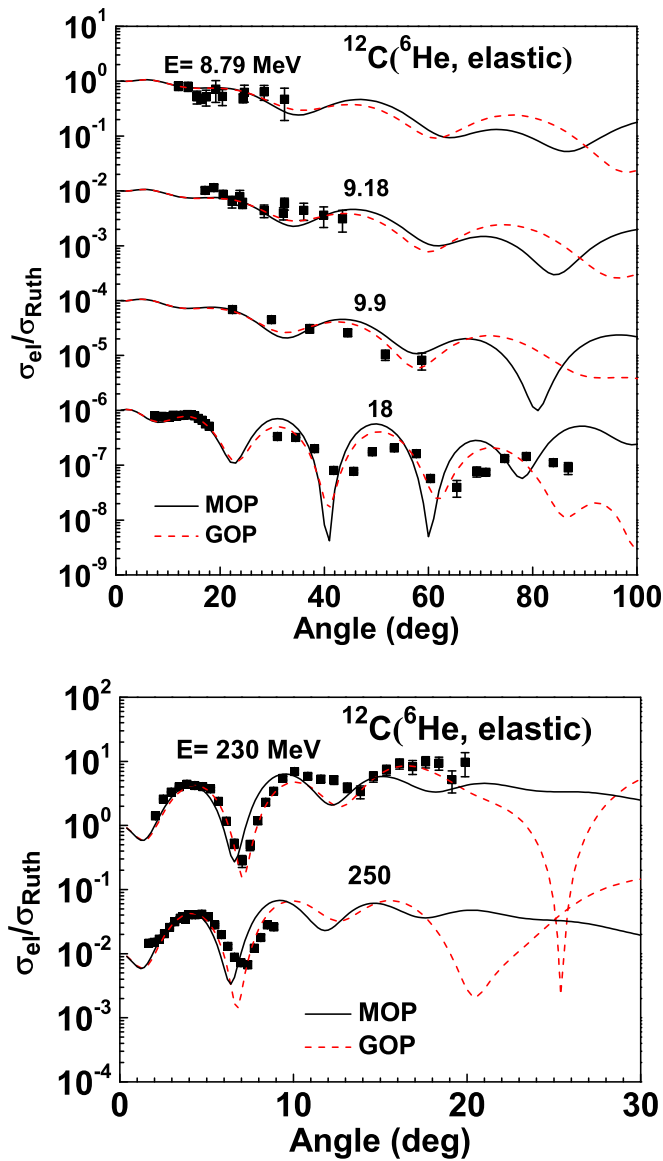


FIG. 4. Calculated differential cross sections relative to Rutherford cross section for  ${}^6\text{He}$  elastic scattering from  ${}^{12}\text{C}$  at incident energies from 8.79 to 250 MeV compared with experimental data. The solid lines and dashed lines denote the results calculated by the MOP and the GOP [22], respectively. The data are shifted downward by factors of  $10^0$ ,  $10^{-2}$ ,  $10^{-4}$ , and so on.

${}^{120}\text{Sn}$  at incident energies from 17.4 to 20.05 MeV is compared with the experimental data [14] in Fig. 10. The calculated result is in basic agreement with the experimental data.

Similar comparisons are made for  ${}^6\text{He}$  elastic scattering from the three heavy nuclei  ${}^{197}\text{Au}$ ,  ${}^{208}\text{Pb}$ , and  ${}^{209}\text{Bi}$  in Figs. 11–13. The experimental data are taken from Refs. [15–20]. Reasonable agreement is obtained in these cases except for back angles. The discrepancies maybe come from the effect of breakup. The breakup effect becomes strong for relatively heavier target nuclei at low incident energies; however, the theoretical model used here does not consider the excitation effect of  ${}^6\text{He}$ .

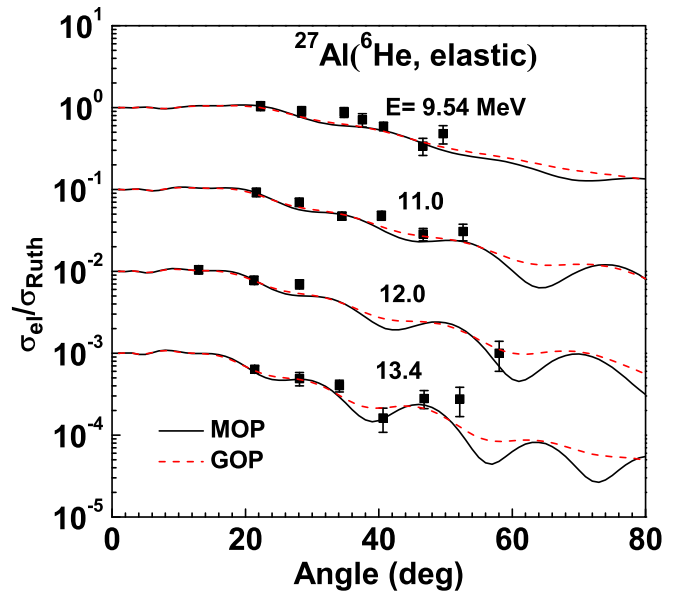


FIG. 5. Same as Fig. 4 but for  ${}^6\text{He}$  elastic scattering from  ${}^{27}\text{Al}$  at incident energies from 9.54 to 13.4 MeV. The data are shifted downward by factors of  $10^0$ ,  $10^{-1}$ ,  $10^{-2}$ , and  $10^{-3}$ .

The experimental data for the total reaction cross section induced by  ${}^6\text{He}$  are very scarce. Warner *et al.* [35] provided a set of experimental data for the  ${}^6\text{He}$ -induced reaction on  ${}^{28}\text{Si}$  at incident energies below 350 MeV. The calculated result is compared with the experimental data in Fig. 14. It can be seen that the calculated result is within the error range of the experimental data.

The  ${}^6\text{He}$  MOP is also used to calculate the differential cross section relative to Rutherford cross section for  ${}^6\text{He}$  elastic scattering from  ${}^9\text{Be}$  at incident energies from 16.2 to 150 MeV. The calculated result is compared with the experimental data [1,2] in Fig. 15. Relatively large discrepancies can be seen.

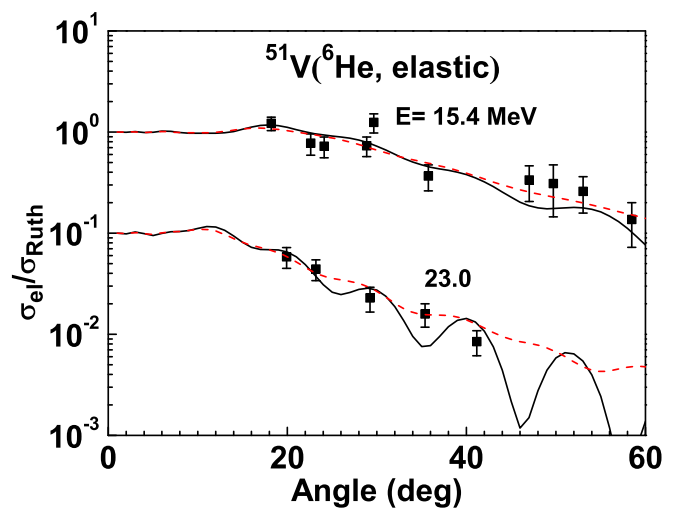


FIG. 6. Same as Fig. 4 but for  ${}^6\text{He}$  elastic scattering from  ${}^{51}\text{V}$  at incident energies of 15.4 and 23.0 MeV. The data are shifted downward by factors of  $10^0$  and  $10^{-1}$ .

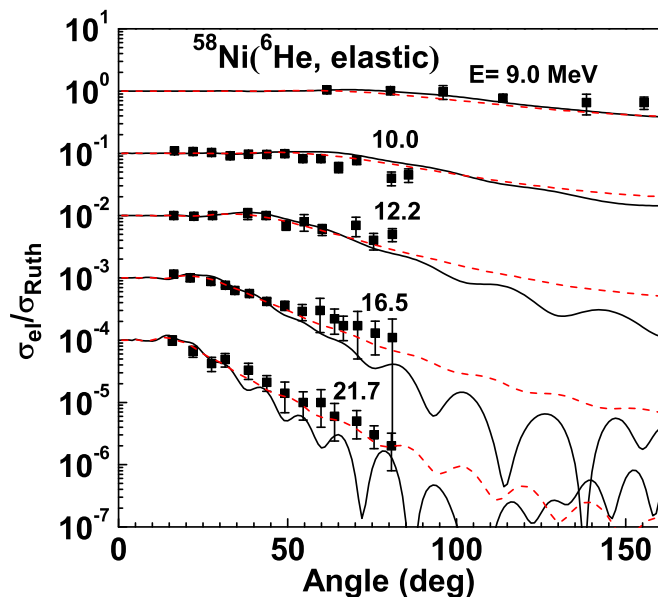


FIG. 7. Same as Fig. 4 but for  ${}^6\text{He}$  elastic scattering from  ${}^{58}\text{Ni}$  at incident energies from 9.0 to 21.7 MeV. The data are shifted downward by factors of  $10^0$ ,  $10^{-1}$ ,  $10^{-2}$ ,  $10^{-3}$ , and  $10^{-4}$ .

The reason for the discrepancies may be that the reaction mechanism is complicated for  ${}^6\text{He} + {}^9\text{Be}$  reaction because  ${}^6\text{He}$  is an unstable light nucleus and  ${}^9\text{Be}$  is a loosely bound light nuclei, which is beyond the range of the predictive ability of the  ${}^6\text{He}$  MOP.

The theoretical results calculated by the  ${}^6\text{He}$  MOP are also compared with those calculated by the GOP from Ref. [22] which are denoted by the dashed lines in the above figures. It can be seen that the GOP results are better than the MOP results in fitting the experimental data generally. It should be

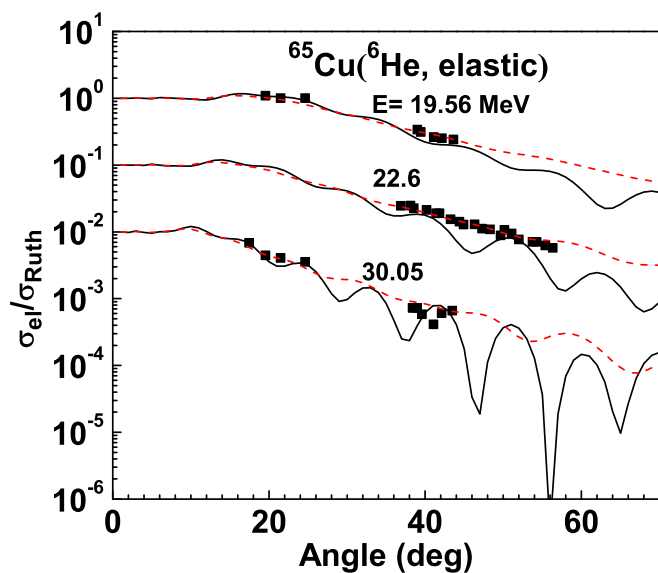


FIG. 8. Same as Fig. 4 but for  ${}^6\text{He}$  elastic scattering from  ${}^{65}\text{Cu}$  at incident energies from 19.56 to 30.05 MeV. The data are shifted downward by factors of  $10^0$ ,  $10^{-1}$ , and  $10^{-2}$ .

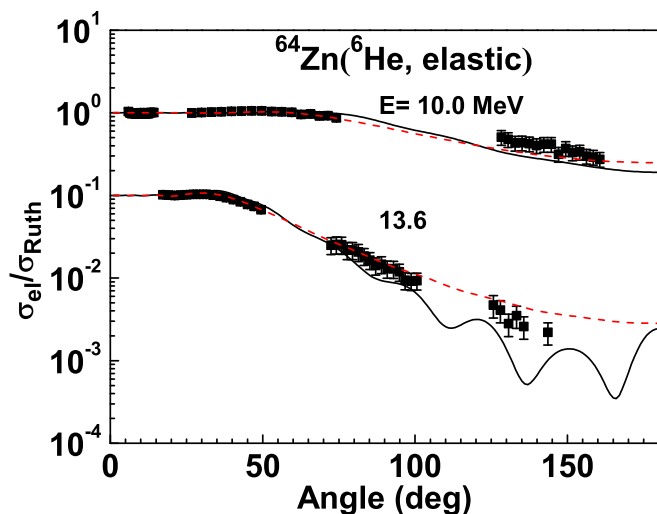


FIG. 9. Same as Fig. 4 but for  ${}^6\text{He}$  elastic scattering from  ${}^{64}\text{Zn}$  at incident energies of 10.0 and 13.6 MeV. The data are shifted downward by factors of  $10^0$  and  $10^{-1}$ .

noted that the GOP is obtained by fitting these experimental data.

To investigate what correction is required to make the MOP give a better global fit, the MOP (solid lines) is compared with the GOP (dashed lines) for the target nucleus  ${}^{209}\text{Bi}$ , as shown in Fig. 16. Because both potentials vary slowly with incident energy, only the case of 22.5 MeV for  ${}^{209}\text{Bi}$  is plotted. It can be seen that the real parts of the two optical potentials are similar, while the imaginary parts are very different. The imaginary part of the GOP has only a surface absorption term, while the imaginary part of the MOP consists of both surface and volume absorption. The sensitivity of scattering to the

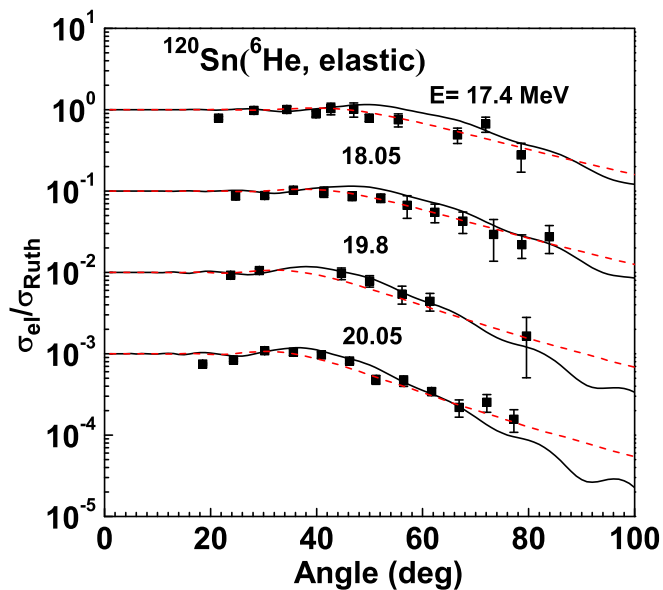


FIG. 10. Same as Fig. 4 but for  ${}^6\text{He}$  elastic scattering from  ${}^{120}\text{Sn}$  at incident energies from 17.4 to 20.05 MeV. The data are shifted downward by factors of  $10^0$ ,  $10^{-1}$ ,  $10^{-2}$ , and  $10^{-3}$ .

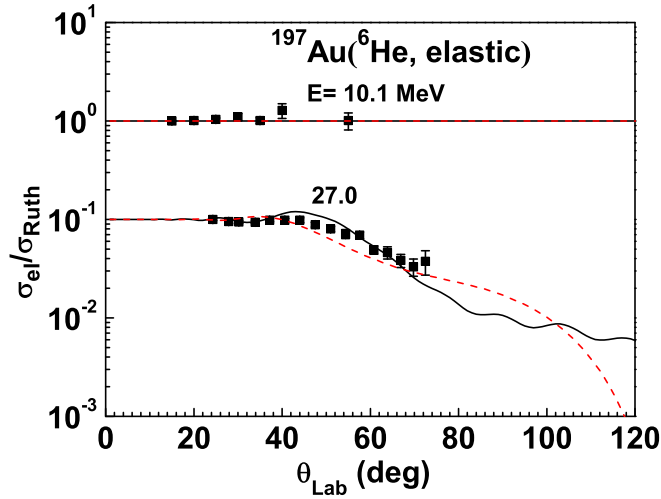


FIG. 11. Same as Fig. 4 but for  ${}^6\text{He}$  elastic scattering from  ${}^{197}\text{Au}$  at incident energies of 10.1 and 27.0 MeV. The data are shifted downward by factors of  $10^0$  and  $10^{-1}$ .

two optical potentials as a function of radius is analyzed by the notch perturbation method [36,37] for this case. The perturbation is performed by reducing the real or imaginary potential to 0 over a region of width 0.5 fm centered at radius  $R$ . The ratio  $\chi^2/\chi_0^2$  is used to judge the sensitivity of scattering to a radial region, where  $\chi^2$  and  $\chi_0^2$  are the chi-squares corresponding to the perturbed and unperturbed potentials, respectively. Figure 17 shows  $\chi^2/\chi_0^2$  for real and imaginary parts of the MOP and GOP. It can be seen that the

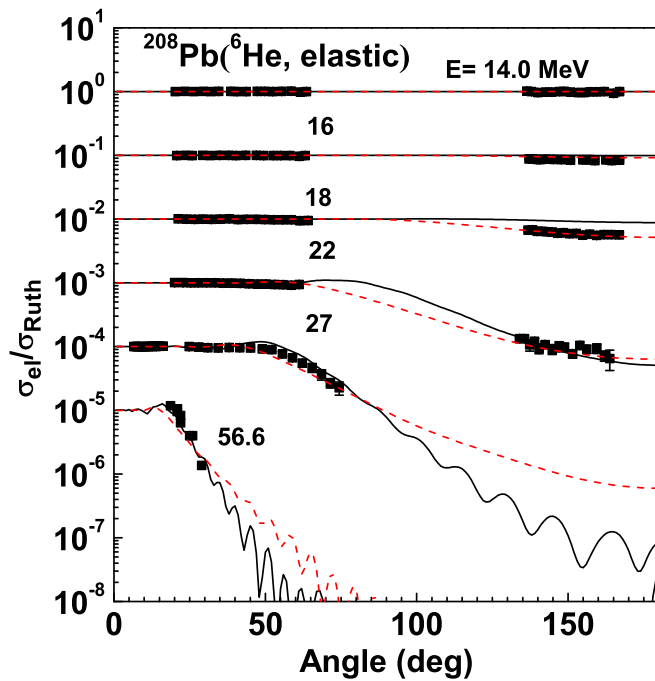


FIG. 12. Same as Fig. 4 but for  ${}^6\text{He}$  elastic scattering from  ${}^{208}\text{Pb}$  at incident energies from 14.0 to 56.6 MeV. The data are shifted downward by factors of  $10^0$ ,  $10^{-1}$ ,  $10^{-2}$ , and so on.

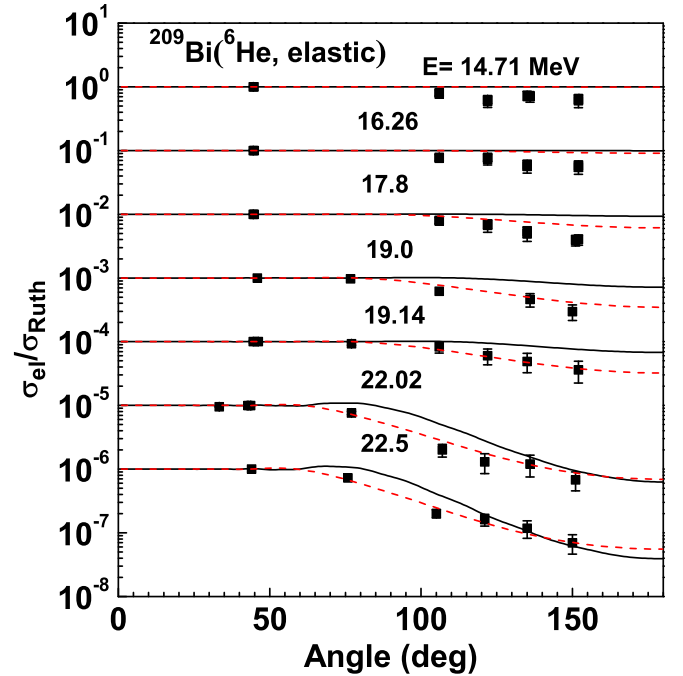


FIG. 13. Same as Fig. 4 but for  ${}^6\text{He}$  elastic scattering from  ${}^{209}\text{Bi}$  at incident energies from 14.71 to 22.5 MeV. The data are shifted downward by factors of  $10^0$ ,  $10^{-1}$ ,  $10^{-2}$ , and so on.

sensitive radial region for the real part of the MOP is 5–14 fm, and the  $\chi^2/\chi_0^2$  nearly remains at unity for the imaginary part of the MOP. In addition, the sensitive radial region for the real part of the GOP is 12–14 fm and for the imaginary part of the GOP it is 11–15 fm. We replace the real part of the MOP by the GOP in the radial region of 5–14 fm and replace the imaginary part of the MOP by the GOP in the radial region of 11–15 fm separately, and get the elastic-scattering angular

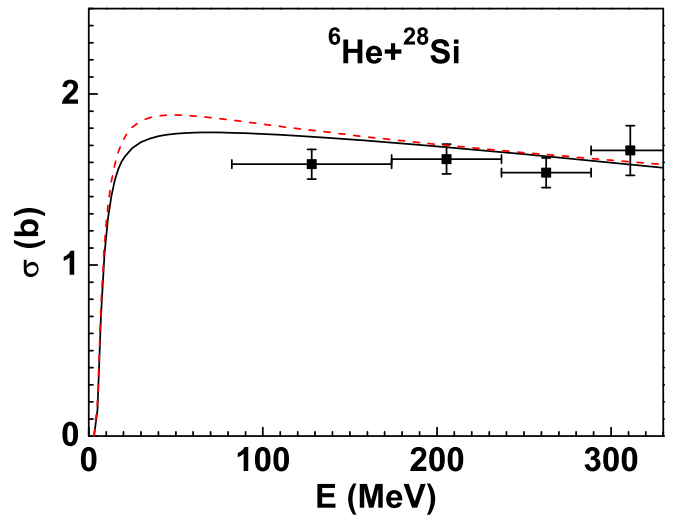


FIG. 14. Calculated total reaction cross sections for  ${}^6\text{He} + {}^{28}\text{Si}$  compared with experimental data. The results calculated by MOP and GOP are denoted by the solid line and dashed line, respectively.

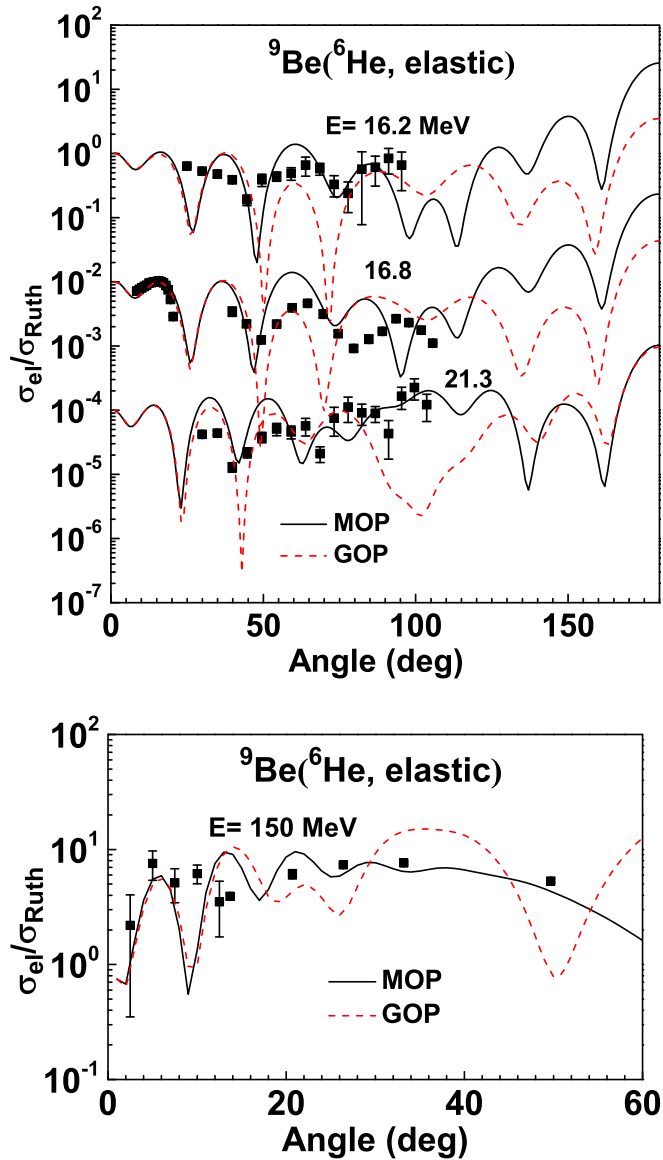


FIG. 15. Same as Fig. 4 but for  ${}^6\text{He}$  elastic scattering from  ${}^9\text{Be}$  at incident energies from 16.2 to 150 MeV. The data are shifted downward by factors of  $10^0$ ,  $10^{-2}$ , and  $10^{-4}$ .

distributions denoted by dash-dot-dotted and dash-dotted lines in Fig. 18, respectively. It can be seen that the calculated result still fails to fit the experimental data in the intermediate-angle region when the real part is replaced, whereas good agreement is obtained when the imaginary part is replaced. This suggests that the surface absorption contribution must be increased in the MOP to get a better global agreement. It is expected that the underestimation of the surface absorption is because the breakup effect is not considered in the derivation of the MOP, which exactly plays its role in the nuclear surface region. The  $\chi^2/\chi_0^2$  for the imaginary part of the MOP increasing very little in the radial region of 11–15 fm is because the imaginary part of the MOP is small in this region, which leads to a weak perturbation.

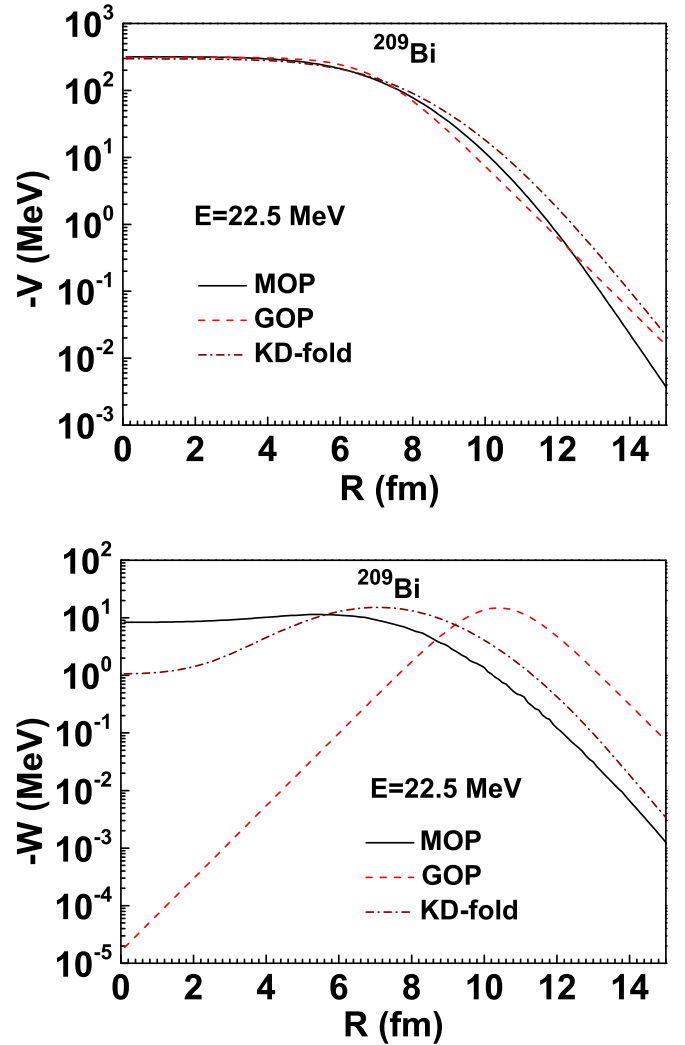


FIG. 16. Comparison of the MOP (solid lines), GOP [22] (dashed lines), and KD-fold (dash-dotted lines) for  ${}^6\text{He} + {}^{209}\text{Bi}$  reaction at the incident energy of 22.5 MeV.

A single-folding potential (KD-fold for short) based on the KD global nucleon potential [38] that is known to work reasonably well and the internal wave function of  ${}^6\text{He}$  given in Sec. II is also obtained and shown by the dash-dotted lines in Fig. 16. It can be seen that the real part is similar to the MOP and GOP, whereas the imaginary part is a little larger than the MOP and less than the GOP in the radial region of 11–15 fm. Figure 19 shows the comparison of calculated elastic-scattering angular distributions using the three optical potentials with the experimental data for  ${}^{209}\text{Bi}$  at 22.5 MeV. The KD-fold result is a little better than the MOP result for the intermediate-angle region and worse for larger angles in fitting the experimental data. The fact that KD-fold also cannot reproduce the experimental data well further indicates that the breakup coupling effect which is not considered in the model is closely related to the discrepancy.

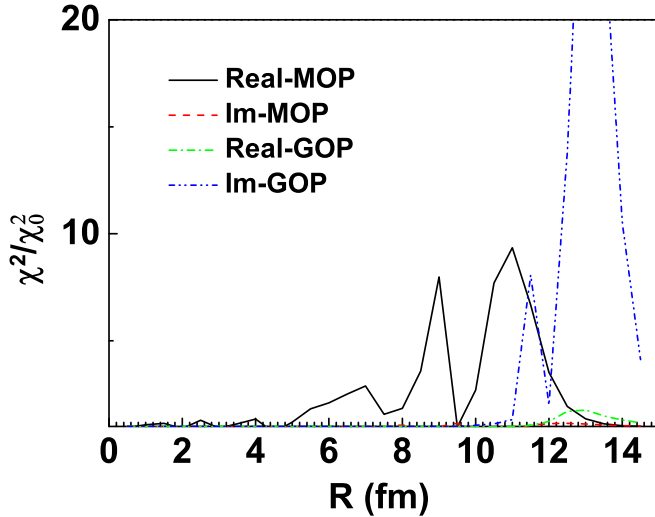


FIG. 17. Radial sensitivity of the differential cross sections of  ${}^6\text{He}$  elastic scattering from  ${}^{209}\text{Bi}$  at the incident energy of 22.5 MeV to the MOP and GOP. The solid and dashed lines show the results of perturbing the real and imaginary parts of the MOP, respectively, while the dash-dotted and dash-dot-dotted lines denote the results of perturbing the real and imaginary parts of the GOP, respectively.

#### IV. SUMMARY

The microscopic optical potential for  ${}^6\text{He}$  with no free parameters is obtained by the folding model. In the model, we use the isospin-dependent nucleon microscopic optical potential, which is derived by using the Green's function method through the nuclear matter approximation and the local density

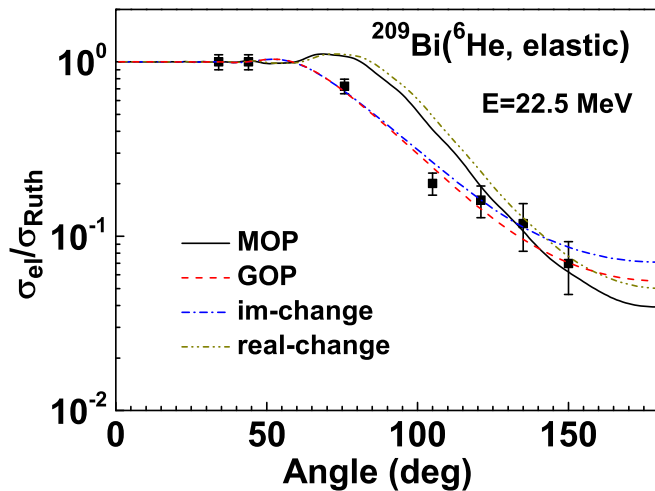


FIG. 18. The differential cross sections relative to Rutherford cross section for  ${}^6\text{He}$  elastic scattering from  ${}^{209}\text{Bi}$  at the incident energy of 22.5 MeV. The solid and dashed lines denote the results calculated by the MOP and GOP [22], respectively. The dash-dot-dotted line denotes the result calculated by the MOP with the real part replaced by the GOP in the radial region of 5–14 fm. The dash-dotted line denotes the result calculated by the MOP with the imaginary part replaced by the GOP in the radial region of 11–15 fm.

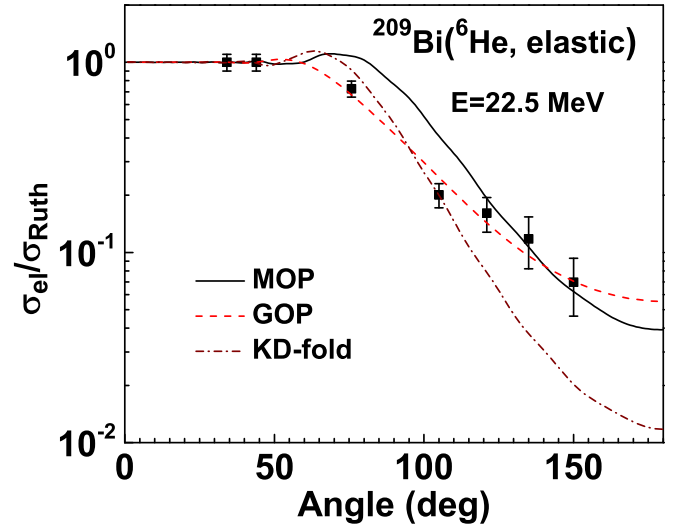


FIG. 19. The differential cross sections relative to Rutherford cross section for  ${}^6\text{He}$  elastic scattering from  ${}^{209}\text{Bi}$  at the incident energy of 22.5 MeV. The solid, dashed, and dash-dotted lines denote the results calculated by the MOP, GOP, and KD-fold, respectively.

approximation based on the Skyrme nucleon-nucleon effective interaction. The probability distribution of the nucleons within  ${}^6\text{He}$  is described by harmonic-oscillator wave function. To check the predictive power and the reliability of the  ${}^6\text{He}$  microscopic optical potential, it is used to calculate the reaction cross sections and elastic-scattering angular distributions for target nuclei in the mass range  $12 \leq A \leq 209$  at incident energies up to 350 MeV, the theoretical results are in reasonable agreement with the experimental data generally except for the medium and heavy nuclei at some relatively larger angles. The predictive ability for lighter target nucleus  ${}^9\text{Be}$  is also checked, and relatively large discrepancy of the calculated results and the experimental data is observed. Therefore, the MOP is not appropriate for target nuclei with mass number less than 12. The theoretical results calculated by the  ${}^6\text{He}$  MOP are also compared with those calculated by the GOP. The GOP can reproduce the experimental data better generally. The radial dependence of the MOP is compared with that of the GOP, and the sensitivity of scattering to the two optical potentials as a function of radius is analyzed by the notch perturbation method. When the imaginary part of the MOP is replaced by the GOP in the sensitive radial region from 11 to 15 fm, good agreement between the theoretical result and the experimental data is obtained. It is concluded from the comparison and discussion that the MOP can be improved by increasing the surface absorption contribution, which is expected to come from the breakup effect.

#### ACKNOWLEDGMENT

This work was supported by the National Natural Science Foundation of China (Grant No. 11175260).

- [1] K. C. C. Pires, R. Lichtenthaler, A. Lepine-Szily, V. Guimaraes, P. N. de Faria, A. Barioni, D. R. Mendes, Jr., V. Morcelle, R. Pampa Condori, M. C. Morais, J. C. Zamora, E. Crema, A. M. Moro, M. Rodriguez-Gallardo, M. Assuncao, J. M. B. Shorto, and S. Mukherjee, *Phys. Rev. C* **83**, 064603 (2011).
- [2] Y. L. Ye, D. Y. Pang, D. X. Jiang, T. Zheng, Q. J. Wang, Z. H. Li, X. Q. Li, Y. C. Ge, C. Wu, G. L. Zhang, Q. Y. Hu, J. Wang, Z. Q. Chen, A. Ozawa, Y. Yamaguchi, R. Kanungo, and I. Tanihata, *Phys. Rev. C* **71**, 014604 (2005).
- [3] M. Milin, S. Cherubini, T. Davinson, A. Di Pietro, P. Figuera, D. Miljanic, A. Musumarra, A. Ninane, A. N. Ostrowski, M. G. Pellegriti, A. C. Shoter, N. Soic, C. Spitaleri, and M. Zadro, *Nucl. Phys. A* **730**, 285 (2004).
- [4] R. J. Smith, J. J. Kolata, K. Lamkin, A. Morsad, K. Ashktorab, F. D. Becchetti, J. A. Brown, J. W. Janecke, W. Z. Liu, and D. A. Roberts, *Phys. Rev. C* **43**, 761 (1991).
- [5] V. Lapoux, N. Alamanos, F. Auger, V. Fekou-Youmbi, A. Gillibert, F. Marie, S. Ottini-Hustache, J. L. Sida, D. T. Khoa, Y. Blumenfeld, F. Marechal, J. A. Scarpaci, T. Suomijarvi, J. H. Kelley, J. M. Casandjian, M. Chartier, M. D. Cortina-Gil, M. MacCormick, W. Mittig, F. de Oliveira Santos, A. N. Ostrowski, P. Roussel-Chomaz, K. W. Kemper, N. Orr, and J. S. Winfield, *Phys. Rev. C* **66**, 034608 (2002).
- [6] J. S. Al-Khalili *et al.*, *Phys. Lett. B* **378**, 45 (1996).
- [7] E. A. Benjamim *et al.*, *Phys. Lett. B* **647**, 30 (2007).
- [8] R. Lichtenthaler *et al.*, *Eur. Phys. J. Spec. Top.* **150**, 27 (2007).
- [9] V. Morcelle *et al.*, *Phys. Lett. B* **732**, 228 (2014).
- [10] L. R. Gasques, L. C. Chamon, D. Pereira, V. Guimaraes, A. Lepine-Szily, M. A. G. Alvarez, E. S. Rossi, Jr., C. P. Silva, B. V. Carlson, J. J. Kolata, L. Lamm, D. Peterson, P. Santi, S. Vincent, P. A. De Young, and G. Peasley, *Phys. Rev. C* **67**, 024602 (2003).
- [11] A. Chatterjee, A. Navin, A. Shrivastava, S. Bhattacharyya, M. Rejmund, N. Keeley, V. Nanal, J. Nyberg, R. G. Pillay, K. Ramachandran, I. Stefan, D. Bazin, D. Beaumel, Y. Blumenfeld, G. de France, D. Gupta, M. Labiche, A. Lemasson, R. Lemmon, R. Raabe, J. A. Scarpaci, C. Simenel, and C. Timis, *Phys. Rev. Lett.* **101**, 032701 (2008).
- [12] A. Navin, V. Tripathi, Y. Blumenfeld, V. Nanal, C. Simenel, J. M. Casandjian, G. de France, R. Raabe, D. Bazin, A. Chatterjee, M. Dasgupta, S. Kailas, R. C. Lemmon, K. Mahata, R. G. Pillay, E. C. Pollacco, K. Ramachandran, M. Rejmund, A. Shrivastava, J. L. Sida, and E. Tryggestad, *Phys. Rev. C* **70**, 044601 (2004).
- [13] A. Di Pietro, P. Figuera, F. Amorini, C. Angulo, G. Cardella, S. Cherubini, T. Davinson, D. Leanza, J. Lu, H. Mahmud, M. Milin, A. Musumarra, A. Ninane, M. Papa, M. G. Pellegriti, R. Raabe, F. Rizzo, C. Ruiz, A. C. Shoter, N. Soic, S. Tudisco, and L. Weissman, *Phys. Rev. C* **69**, 044613 (2004).
- [14] P. N. de Faria, R. Lichtenthaler, K. C. C. Pires, A. M. Moro, A. Lepine-Szily, V. Guimaraes, D. R. Mendes, Jr., A. Arazi, M. Rodriguez-Gallardo, A. Barioni, V. Morcelle, M. C. Morais, O. Camargo, Jr., J. Alcantara Nunez, and M. Assuncao, *Phys. Rev. C* **81**, 044605 (2010).
- [15] O. R. Kakuee *et al.*, *Nucl. Phys. A* **765**, 294 (2006).
- [16] A. M. Sanchez-Benitez *et al.*, *J. Phys. G* **31**, S1953 (2005).
- [17] A. M. Sanchez-Benitez *et al.*, *Nucl. Phys. A* **803**, 30 (2008).
- [18] N. K. Skobelev *et al.*, *Z. Phys. A: Hadrons Nucl.* **341**, 315 (1992).
- [19] E. F. Aguilera, J. J. Kolata, F. D. Becchetti, P. A. De Young, J. D. Hinnefeld, . Horvath, L. O. Lamm, H.-Y. Lee, D. Lizcano, E. Martinez-Quiroz, P. Mohr, T. W. O'Donnell, D. A. Roberts, and G. Rogachev, *Phys. Rev. C* **63**, 061603(R) (2001).
- [20] E. F. Aguilera, J. J. Kolata, F. M. Nunes, F. D. Becchetti, P. A. De Young, M. Goupell, V. Guimaraes, B. Hughey, M. Y. Lee, D. Lizcano, E. Martinez-Quiroz, A. Nowlin, T. W. O'Donnell, G. F. Peaslee, D. Peterson, P. Santi, and R. White-Stevens, *Phys. Rev. Lett.* **84**, 5058 (2000).
- [21] Y. Kucuk, I. Boztosun, and T. Topel, *Phys. Rev. C* **80**, 054602 (2009).
- [22] X. Su *et al.*, *Int. J. Mod. Phys. E* **25**, 1650033 (2016).
- [23] Q.-b. Shen, Y.-l. Han, and H.-r. Guo, *Phys. Rev. C* **80**, 024604 (2009).
- [24] H. Guo, Y. Xu, Y. Han, and Q. Shen, *Phys. Rev. C* **81**, 044617 (2010).
- [25] H. Guo, Y. Xu, H. Liang, Y. Han, and Q. Shen, *Nucl. Phys. A* **922**, 84 (2014).
- [26] H. Guo, Y. Zhang, Y. Han, and Q. Shen, *Phys. Rev. C* **79**, 064601 (2009).
- [27] H. Guo, Y. Xu, H. Liang, Y. Han, and Q. Shen, *Phys. Rev. C* **83**, 064618 (2011).
- [28] S. Watanabe, *Nucl. Phys.* **8**, 484 (1958).
- [29] F. G. Perey and G. R. Satchler, *Nucl. Phys. A* **97**, 515 (1967).
- [30] S. K. Samaddar and R. K. Satpathy, *Nucl. Phys. A* **150**, 655 (1970).
- [31] J. S. Bell and E. J. Squires, *Phys. Rev. Lett.* **3**, 96 (1959).
- [32] S. Krewald, V. Klemt, J. Speth, and A. Faessler, *Nucl. Phys. A* **281**, 166 (1977).
- [33] J. W. Negele, *Phys. Rev. C* **1**, 1260 (1970).
- [34] L. V. Chulkov, B. V. Danilin, V. D. Efros, A. A. Korshennikov, and M. V. Zhukov, *Europhys. Lett.* **8**, 245 (1989).
- [35] R. E. Warner, R. A. Patten, P. M. Voyles, A. Nadasen, F. D. Becchetti, J. A. Brown, H. Esbensen, A. Galonsky, J. J. Kolata, J. Kruse, M. Y. Lee, R. M. Ronningen, P. Schwandt, J. von Schwarzenberg, B. M. Sherrill, K. Subotic, J. Wang, and P. Zecher, *Phys. Rev. C* **54**, 1700 (1996).
- [36] P. J. Moffa, C. B. Dover, and J. P. Vary, *Phys. Rev. C* **13**, 147 (1976).
- [37] J. G. Cramer and R. M. DeVries, *Phys. Rev. C* **22**, 91 (1980).
- [38] A. J. Koning and J. P. Delaroche, *Nucl. Phys. A* **713**, 231 (2003).